Identification of vibrational mode symmetry and phonon anharmonicity in SbCrSe3 single crystal using Raman spectroscopy

Hong Wu, Xiangnan Gong, Yi Peng, Long Zhang, Bin Zhang, Kunling Peng, Jie Liu, Guang Han, Aifeng Wang, Yisheng Chai, et al.

SCIENCE CHINA Materials

Identification of vibrational mode symmetry and phonon anharmonicity in $SbCrSe_3$ single crystal using Raman spectroscopy

Hong Wu[1,2,†], Xiangnan Gong[3,†], Yi Peng[4], Long Zhang[1], Bin Zhang[3], Kunling Peng[1], Jie Liu[3], Guang Han[5], Aifeng Wang[1], Yisheng Chai[1], Mingquan He[1], Haoshuang Gu[4], Emmanuel Guilmeau[6], Guoyu Wang[2,*], Xu Lu[1,*] and Xiaoyuan Zhou[1,3,*]

[1] College of Physics and Institute of Advanced Interdisciplinary Studies, Chongqing University, Chongqing 401331, China

[2] Chongqing Institute of Green and Intelligent Technology, Chinese Academy of Sciences, Chongqing 400714, China

[3] Analytical and Testing Center of Chongqing University, Chongqing 401331, China

[4] Hubei Collaborative Innovation Center for Advanced Organic Chemical Materials, Hubei Key Laboratory of Ferro & Piezoelectric Materials and Devices, Faculty of Physics & Electronic Sciences, Hubei University, Wuhan 430062, China

[5] College of Materials Science and Engineering, Chongqing University, Chongqing 400044, China

[6] Laboratoire CRISMAT, UMR-CNRS, Normandie University, Caen 14050, France

[†] These authors contributed equally to this work.

[*] Corresponding authors (emails: guoyuw@cigit.ac.cn (Wang G); luxu@cqu.edu.cn (Lu X); xiaoyuan2013@cqu.edu.cn (Zhou X))

ABSTRACT

Understanding the underlying physics of vibrational phonon modes, which are strongly related to thermal transport, has attracted significant research interest. Here, we report the successful synthesis of bulk $SbCrSe_3$ single crystal and its thermal transport property over the temperature range from 2 K to 300 K. Using angle-resolved polarized Raman spectroscopy (ARPRS) and group theory calculation, the vibrational symmetry of each observed Raman mode in the cleaved (00l) crystal plane of $SbCrSe_3$ is identified for the first time, and further verified by first-principles calculations. Meanwhile, the ARPRS results of some Raman modes (e.g., A_g^2 ~64 cm^{-1} and A_g^7 ~185 cm^{-1}) can be adopted to determine the crystalline orientation. More importantly, it is revealed that the temperature dependence of the lattice thermal conductivity (κ_L) is more accurately depicted by the three-phonon scattering processes throughout the measured temperature range, substantiated by the *in-situ* Raman spectroscopy analysis and the model-predicted κ_L. These results disclose the fundamental physics of thermal transport for $SbCrSe_3$ from a completely new perspective and thus should ignite the research interests in thermal properties of other low dimensional materials by using the same strategy.

Keywords: $SbCrSe_3$ single crystal, in-situ Raman, angle-resolved polarized Raman spectroscopy, lattice dynamics, thermal transport

INTRODUCTION

Low-dimensional bulk materials, with quasi one-dimensional (1D) or 2D structure, have been received growing attention owing to the extraordinary electronic and thermal properties, and emerged as highly attractive candidates used for next-generation electronic, optoelectronic and thermoelectric devices [1–8]. In particular, the low dimensional intrinsic magnetic semiconductors, $CrMX_3$ ternary chromium trichalcogenides (M as a non-transition metal and X = S, Se or Te), have garnered wide interests in magnetism and thermoelectricity fields due to appropriate band gap and intrinsically low κ_L [9–15]. Intriguingly, the crystal structure of these compounds, by virtue of the different arrangement of CrX_6 octahedra, can transform from quasi-2D layered structure to 1D needlelike structure. For example, $CrMX_3$ holds a laminar structure when M = Si, Ge, or Sn, with CrX_6 octahedra adopting a honeycomb lattice; in contrast, when Sb or Ga appears on M sites, it exhibits a pseudo-1D crystal structure, with CrX_6 octahedra forming infinite, edge-sharing and double rutile chains, in which M atoms are linked to the neighboring chains. The relative angle between the double rutile chains is determined by the type of M atoms [16]. Although the crystal structures of these compounds have been fully comprehended, the advancement of investigation on their fundamental lattice vibration properties is still relatively slow.

Raman spectrum, as a fast and nondestructive tool, has been widely employed to characterize the phonon characteristics in the vicinity of Brillouin zone center, the crystal structure, and electron-phonon interactions, especially in many low dimensional materials [17–20]. As a characteristic example of $CrMX_3$ compounds, $SbCrSe_3$ has an orthorhombic structure with 20 atoms in its primitive cell and is subject to the *Pnma* space group and D_{2h} point group. Based on the group analysis, 60 vibrational modes at the Γ point in Brillouin zone are expectantly generated, in which eight inequivalent irreducible are included in the D_{2h} point group as following: $\Gamma = 10A_g + 5B_{1g} + 10B_{2g} + 5B_{3g} + 5A_u + 10B_{1u} + 5B_{2u} + 10B_{3u}$. One can see that the symmetries of 30 Raman active modes, including $10A_g + 5B_{1g} + 10B_{2g} + 5B_{3g}$, are predicted by

group theory. Recently, the ARPRS has emerged as a powerful tool to resolve and assign Raman modes symmetries for some important crystals, and to determine the crystalline orientation of films and nanotubes [21–24]. However, to the best of our knowledge, such a technique has never been employed to identify the vibrational symmetries for the experimentally observed Raman modes in the low dimensional $CrMX_3$ semiconductors.

Moreover, $SbCrSe_3$ exhibits intrinsically low κ_L [15], indicating that it could be a promising thermoelectric material after electrical property optimization [25–30]. Nevertheless, the underlying physics for the low thermal conductivity of $SbCrSe_3$, which relies on the analysis of phonon modes, is still obscure until now. By virtue of *in-situ* Raman spectroscopy analysis, the temperature-dependent lattice vibration characteristics can be precisely attained, which further illustrates the anharmonic interactions between phonons by analyzing the temperature-dependent evolution of Raman peaks and corresponding full width at half maximum (FWHM) [31–33]. Hence, it is essential to unveil the phonon scattering mechanisms in bulk low dimensional materials like $SbCrSe_3$ using the combination of *in-situ* Raman experiment and lattice dynamics.

In this study, we report the determination of mode symmetry for each observed Raman peak in $SbCrSe_3$ single crystal. It is found that three-phonon scattering processes dominate the thermal transport for $SbCrSe_3$ throughout the measured temperature range, as suggested by the temperature dependence of Raman mode frequency and linewidth, which is further corroborated by the good consistency between experimental and calculated thermal conductivity. Our findings highlight the utilization of Raman spectrum as a fast, precise, and nondestructive method to identify the vibrational modes symmetry, crystalline orientation and the phonon anharmonicity for low dimensional materials.

EXPERIMENTAL AND THEORETICAL METHODS

Synthesis

$SbCrSe_3$ single crystals were grown by self-flux method. Starting elements (chunks, 99.99%, Sigma-Aldrich) were weighted according to a molar ratio of Cr:Sb:Se = 2:38:60 and loaded into an alumina crucible. The alumina crucible was placed into a quartz tube, and another alumina crucible with silica wool was placed upside down on the prior one. Then, the quartz tube was evacuated to a pressure of 5×10^{-4} Pa and sealed. Quartz tubes were heated up to 1000 K over 12 h, slowly cooled to 900 K and remained at this temperature for 144 h; after that, the molten liquid was separated from the crystals in a centrifuge, with silica wool serving as a filter. Finally, the obtained needle crystals were evacuated, encapsulated in fused quartz tube, and annealed at 780 K for 24 h. Consequently, millimeter-long malleable single crystals of $SbCrSe_3$ were obtained.

Characterizations

Diffraction intensity data of single crystal $SbCrSe_3$ were collected on an Agilent Technologies SuperNova single-crystal X-ray diffraction (SCXRD) at 295 K equipped with graphite-monochromatic Mo Kα radiation (λ = 0.71073 Å). The structures were solved with the SHELXT structure solution program and refined with SHELXL refinement package. XRD pattern was recorded *via* a PANalytical X-ray diffractometer that was operated at 40 kV and 40 mA using Cu Kα (λ = 1.5418 Å) radiation. Raman spectra measurements were carried out by HORIBA JobinYvon HR Evolution, and 600 and 1800 groove mm^{-1} holographic grating combining with thermoelectric cooled Synapse charge coupled device were used for the ARPRS and temperature dependent Raman experiments, respectively. Solid-state Nd:YAG laser with the wavelength of 532 nm was used as the excitation source. The thermal conductivity was measured in Physical Property Measurement System (PPMS) DynaCool 9. The high-resolution transmission electron microscopy (HRTEM) and scanning transmission electron microscopy high-angle annular dark field (STEM-HAADF) were employed to characterize microstructure. The corresponding energy-dispersive X-ray spectroscopy

(EDX) mapping was acquired on a transmission electron microscope (Talos F200S G2) operating at 200 kV. Electron probe micro-analyzer (EPMA, JXA-8530F Plus, JEOL, Japan) was used to determine the distribution of Sb, Cr and Se in the single crystal with a spatial resolution of 1 μm.

DFT calculations

Under the precondition of density functional theory (DFT) [34], the Vienna *ab-initio* Simulation Package (VASP) code using the projector augmented plane wave (PAW) methods is implemented for all calculations [35]. A generalized gradient approximation (GGA) of Perdew-Burke-Ernzerhof (PBE) is defined as the relevant exchange-correlation functional [36]. For the relaxation of the crystal structure, the total energies of electronic self-consistent interactions were numerically converged to 1×10^{-8} eV with a basis set energy cutoff of 600 eV for and the forces on the atoms were 1×10^{-4} eV Å^{-1} for optimizing the atomic positions. For the Brillouin zone integrations, the k-mesh grid ($5 \times 11 \times 3$) centered at Γ was used for the primitive cell. To calculate phonon dispersion, the finite displacement methods using $2 \times 3 \times 1$ supercell were performed in Phonopy package to investigate the lattice dynamics of $SbCrSe_3$ [37]. Furthermore, the κ_L was calculated by ShengBTE package using a cutoff of 10 angstrom for the interaction range and $1 \times 3 \times 1$ supercell to obtain third order anharmonic inter atomic force constants (IFCs) [38].

RESULTS AND DISCUSSION

Phase characterization

The structure of our $SbCrSe_3$ single crystal, with the lattice parameters a = 9.1475(6) Å, b = 3.7872(3) Å and c = 13.4264(11) Å obtained by the refinement of SCXRD, is orthorhombic with *Pnma* space group (No. 62) and D_{2h} point group. Structural data are displayed in Table S1. Fig. 1a shows the refined crystal structure of $SbCrSe_3$, which is regarded as a quasi-1D structure with double chains of $CrSe_6$ octahedra aligned parallel to the *b*-axis shown in Fig. 1b. Within the double chain, the Cr cations follow an edge-sharing triangular arrangement and Sb atoms are linked to the adjacent chains, resulting in the pseudo-1D crystal structure. As revealed in Fig. 1c, the bond distances between Cr and Se atoms in these octahedra range from 2.5301 to 2.5949 Å, leading to the slightly distorted octahedron due to the asymmetric chemical bond lengths, and the Sb-Se1 and Sb-Se2 bond distances are 2.6486 and 2.6714 Å, respectively. The synthesized $SbCrSe_3$ single crystal in Fig. 1d exhibits an aciculiform with a length of ~10 mm along the *b*-axis. The inset graph in Fig. 1e depicts the surface morphology along mirror side. The predominant (00l) diffraction peaks indicate that the *c*-axis is perpendicular to mirror side, which is employed to acquire other data in this work. Moreover, the XRD pattern in Fig. 1e of $SbCrSe_3$ sample (crushed single crystal) is in agreement with previous report (PDF#50-0853), in which no distinct secondary phase is detected.

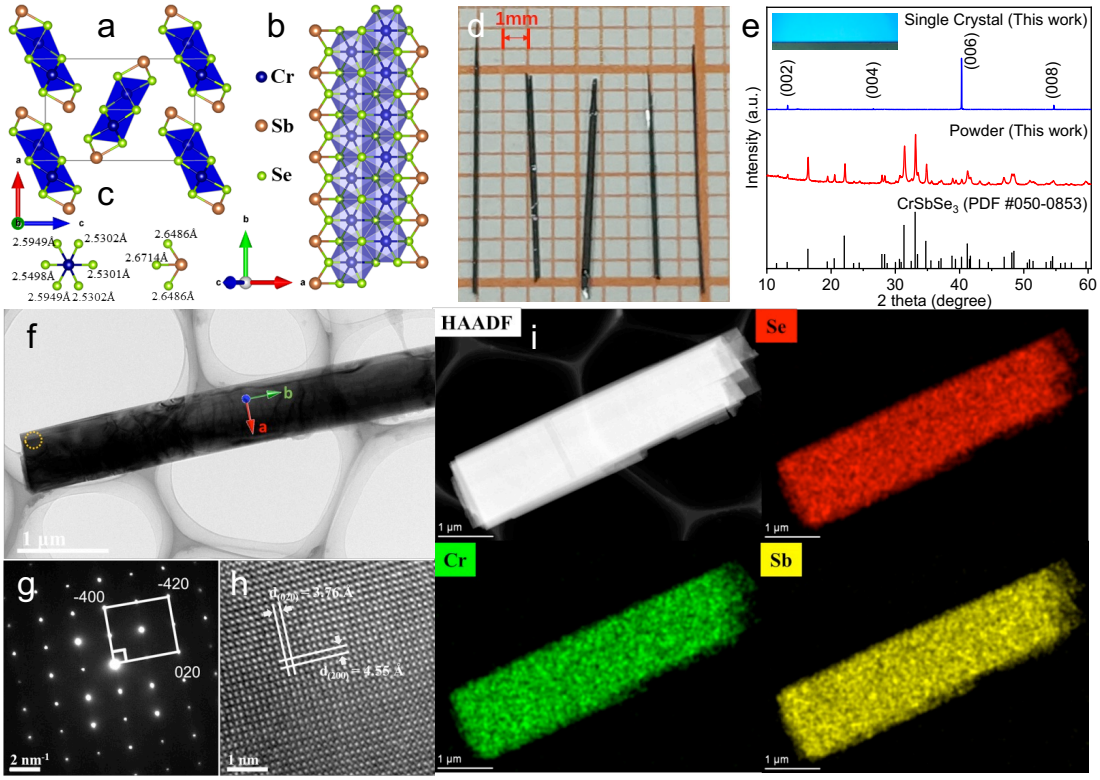

Figure 1 Structural analyses and characterization of $SbCrSe_3$ single crystal. (a) The crystal structure of $SbCrSe_3$ along the *b*-axis. (b) $CrSe_6$ double chains along *b*-axis. (c) Bond lengths from Cr to Se and Sb to Se. (d) The $SbCrSe_3$ crystal, the *b*-axis, is along the long crystal dimension, which is about 10 mm. (e) XRD patterns for $SbCrSe_3$ comparing with PDF#50-0853 and single-crystal $SbCrSe_3$ shows predominantly (00l) peaks. The inset shows the image for single crystal $SbCrSe_3$ used for powder XRD. (f) The HRTEM image of $SbCrSe_3$ along [001] zone axis. The corresponding selected-area electron diffraction pattern and HRTEM image for (g) and (h), respectively. (i) The STEM-HAADF image and the corresponding EDX mapping demonstrates the chemical homogeneity of the $SbCrSe_3$ crystal.

Furthermore, to gain in-depth insight into the structural characterization and the relative orientation of the cleaved (00l) crystal plane of $SbCrSe_3$ crystal, the STEM-HAADF imaging, electron diffraction and EDX mapping were utilized. As displayed in Fig. 1g and h, the clear lattice fringe, in conjunction with the distinguishable fast Fourier transformation (FFT) image, implies the single crystalline feature. Interestingly, the Miller index of the diffraction spot and the measured interplanar distance, marked in Fig. 1g and h, respectively, elucidate the orientation of the long and short edges

shown in Fig. 1g are [020] and [200], respectively, which establishes that the preferred orientation of long edges for cleaving plane of $SbCrSe_3$ crystal is *b*-axis. In addition, the EDX mapping for the synthetic $SbCrSe_3$ sample in Fig. 1i confirms the uniform distribution of Sb, Cr and Se elements, which shows excellent consistency with the results from the EPMA in the regions as displayed in Fig. S1.

Identifying Raman modes symmetries

Raman spectrum not only contains rich information of phonon properties near the Brillouin zone, but also is closely correlated with crystal structures in terms of symmetry. Here, to determine the phonon vibrational symmetries for the Raman modes and relevant anisotropy, the backscattering geometry ARPRS measurement was performed on the cleaved (00l) crystal plane of the $SbCrSe_3$ crystal at room temperature (the schematic of experimental setup is exhibited in Fig. S2). The *a*-axis and *b*-axis of the $SbCrSe_3$ crystal were defined as the x' and y' directions, respectively, as shown in Fig. S2c. Fig. S2a and b separately display the two configurations for the ARPRS experiment, where the green rectangle symbolizes the sample, the red arrow indicates the polarization direction of the incident laser, and the blue one represents the original polarization of Raman backscattered signal from the sample surface corresponding to the analyzer-selected vertical or horizontal direction (denoted as perpendicular (⊥) or parallel (||) polarization configuration, respectively). Fig. 2a displays the Raman spectra of $SbCrSe_3$ single crystal measured in the cleaved (00l) crystal plane at an angle of 0° using un-, parallel-, and perpendicular-polarized configurations. Fourteen Raman modes can be obviously observed under unpolarized configuration. With regard to the under ⊥ and || polarization configurations, however, the peak intensity of some vibrational modes can be enhanced, reduced or even disappeared periodically, which indicates the existence of polarization-dependent behavior.

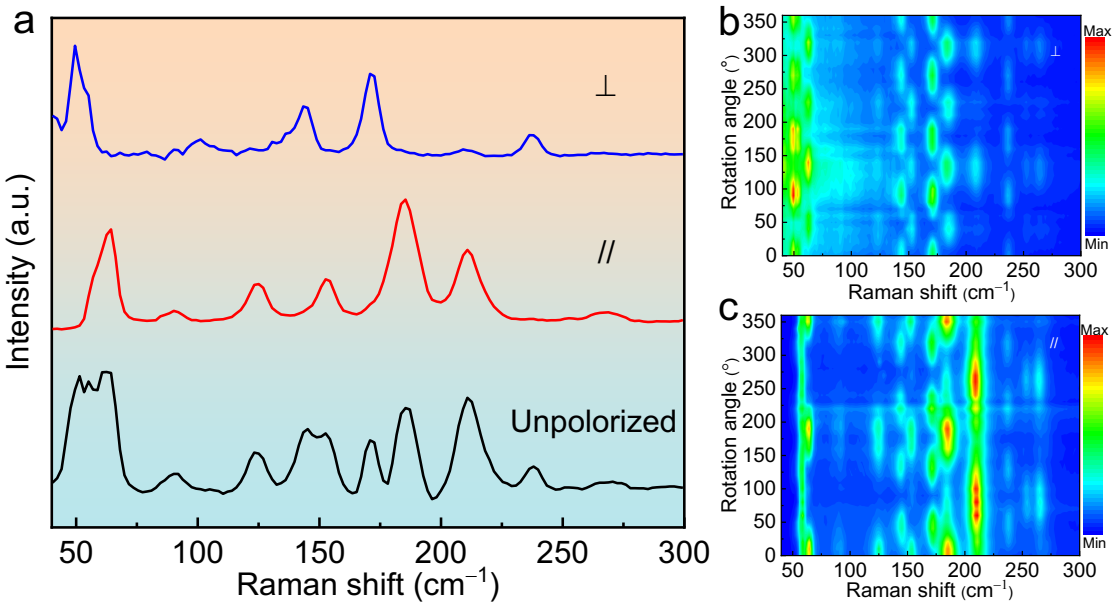

Figure 2 The ARPRS of $SbCrSe_3$. (a) Measuring Raman spectra at angle of 0° under perpendicular (||), parallel (⊥) and un-polarized configurations. False-color plots of polarized Raman intensity under (b) cross and (c) parallel polarization configurations, respectively.

Under cross-polarized configuration, the typical polarized Raman spectra and false-color diagram with the rotation angle from 0° to 360° are shown in Fig. S3a and Fig. 2b, respectively. Interestingly, in this configuration, all modes peak intensities varying with sample rotation have a periodicity of 90° to present 4-lobed shape: some modes have maximum intensities corresponding to angles at 0°, 90°, 180°, and 270° (such as 49, 144, 172 and 238 cm^{-1}) and some at 45°, 135°, 225°, and 315° (e.g., 64, 125, 153, and185 cm^{-1}). In contrast, in parallel-polarized configuration (Fig. S3b and Fig. 2c), some Raman modes intensities repeat after 180°, leading to 2-lobed shape (e.g., 64, 125, 185 and 254 cm^{-1}), which could be employed to estimate the crystalline orientation (along *a* or *b*-direction) of the cleaved (00l) in-plane of $SbCrSe_3$ (as discussed later). Some modes have a 90° variation period, exhibiting 4-lobed shape (e.g., 49, 144, 172 and 238 cm^{-1}). These results clearly uncover not only the anisotropic optical feature of $SbCrSe_3$ crystal but also the dependence of polarized Raman spectrum on crystalline orientation.

On the basis of group theory calculation, the sample angle dependent intensities of each Raman active mode in different crystal planes of the $SbCrSe_3$ sample are full evaluated, which is fundamentally important to identify the mode symmetries. The following calculations are suitable for the analysis of the cleaved (00l) crystal plane and the results of the remaining crystal faces are included in supplementary information (SI Section I). When the (00l) plane of the crystal in the x-y plane is rotated, there is an angle θ between laboratory coordinates (xyz) and crystal coordinates ($x'y'z'$). Raman tensors ($\vec{R}$) of a crystal are defined according to its crystal coordinates, and the laboratory coordinates can be converted as ($\overrightarrow{R'}$) by $\overrightarrow{R'} = \vec{M} \cdot \vec{R} \cdot \vec{M}^{-1}$, where $\vec{M}$ is defined as the orthogonal transform matrix to link the two coordinates:

$$\begin{pmatrix} x \\ y \\ z \end{pmatrix} = \vec{M} \begin{pmatrix} x' \\ y' \\ z' \end{pmatrix}, \quad \vec{M} = \begin{pmatrix} cos\theta & sin\theta & 0 \\ -sin\theta & cos\theta & 0 \\ 0 & 0 & 1 \end{pmatrix} \tag{1}$$

The intensity (I) of the observed Raman vibration modes can be expressed as:

$$\mathrm{I} \propto \left| \vec{e}_i \cdot \vec{M} \cdot \vec{R} \cdot \vec{M}^{-1} \cdot \vec{e}_s \right|^2 \tag{2}$$

where $\vec{e}_s$ and $\vec{e}_i$ are the unit polarization vectors of scatter and incident laser, respectively. The incident laser with unit polarization vector along y-axis ($\vec{e}_i = (0\ 1\ 0)$) propagates along the $\bar{z}$-direction to impinge on the sample. The scattered Raman signal is collected through the selectivity analyzer with unit polarization vector $\vec{e}_s{}^{\mathrm{T}} = (1\ 0\ 0)$ defined as perpendicular configuration and $\vec{e}_s{}^{\mathrm{T}} = (0\ 1\ 0)$ as parallel configuration. For an absorptive material, the Raman tensor elements are complex numbers, with real and imaginary parts [23,39]. Thus, the Raman tensor of A_{g} and $B_{1\mathrm{g}}$ (other modes $B_{2\mathrm{g}}$ and $B_{3\mathrm{g}}$ seeing SI Section I) according to the $D_{2\mathrm{h}}$ point group can be expressed as [39]:

$$\vec{R}(A_{\mathrm{g}}) = \begin{pmatrix} ae^{i\varphi_a} & 0 & 0 \\ 0 & be^{i\varphi_b} & 0 \\ 0 & 0 & ce^{i\varphi_c} \end{pmatrix}, \quad \vec{R}(B_{1\mathrm{g}}) = \begin{pmatrix} 0 & de^{i\varphi_d} & 0 \\ de^{i\varphi_d} & 0 & 0 \\ 0 & 0 & 0 \end{pmatrix} \tag{3}$$

The Raman scattering intensities of different modes can further be expressed as:

$$\mathrm{I}(A_{\mathrm{g}}, \perp) \propto \frac{1}{4} \cdot sin^2 2\theta \cdot (|a|^2 - 2|a||b| \cdot cos\varphi_{ab} + |b|^2) \tag{4}$$

$$\mathrm{I}(A_g, \|) \propto |a|^2 \cdot sin^4\theta + |b|^2 \cdot cos^4\theta + 2|a||b| \cdot cos\varphi_{ab} \cdot sin^2\theta \cdot cos^2\theta \quad (5)$$

$$\mathrm{I}(B_{1g}, \perp) \propto d^2 \cdot cos^2 2\theta \quad (6)$$

$$\mathrm{I}(B_{1g}, \|) \propto d^2 \cdot sin^2 2\theta \quad (7)$$

where $\|$ and $\perp$ represent parallel and perpendicular polarizations, respectively, and $\varphi_{ab} = \varphi_a - \varphi_b$ is the phase difference. Consequently, the relations between I and θ based on group theory analysis for all Raman active modes of $SbCrSe_3$ are summarized in Table S2. Notably, the calculated Raman scattering intensities of the B_{xg} (x = 1–3) modes, independent with the phase difference φ, are only determined by the real parts. Moreover, when the direction of incident laser is perpendicular to the (00l) surface, only Raman-active A_g and B_{1g} modes can be detected.

In parallel polarizer configuration, it is interesting to note that the angular dependence of the A_g intensity with a periodicity of 180° is different from that of B_{1g} modes holding 90° periodicity out of the 2θ dependence. In perpendicular-polarized geometry, though both A_g and B_{1g} modes have similar 90° variation period, the A_g modes intensity as a function of 2θ show sine-like feature and the relation of B_{1g} modes exhibit cosine-like behavior. Thus, the distinguished difference in periodicity or functional relationship (I *versus* 2θ) in these modes is highly beneficial to assign experimental Raman-active modes symmetry. As can be seen from Table S3, the fitting curves according to Eqs. (4)–(7) show excellent consistency with the experiment data. All B_{1g} modes marked by the red lines in both configuration and A_g modes (the blue lines) under cross-polarized geometry show expected 4-lobed shape, and significantly A_g modes under parallel polarizer configuration exhibit 2-lobed shapes. Unambiguously, the symmetry of experimentally observed vibrational modes can be well confirmed, which results from the reliable fitting and complementary results for both configurations. Furthermore, in parallel polarized configuration, the intensities

of some modes (e.g., ~64 and ~185 cm^{-1}) with a periodicity of 180° reach the maximum values at 0° or 180° along *b*-axis and obtain their minimum at 90° and 270° along *a*-axis. Such characteristics could be used as a guide to verify the desirable crystalline orientation of small crystal or films [20,21].

For a better understanding and further verification of these modes assigned to corresponding vibrational symmetry, the phonon dispersion curves along the high symmetry point directions and the vibrational symmetry of phonons vertically intersected with the phonon bands at the *Γ* point in Brillouin zone were calculated. As shown in Fig. 3a, the calculated phonon dispersion of $SbCrSe_3$ along the high symmetry path is absent of imagine frequency, which hints that the calculated lattice structure is thermodynamically stable. Due to the large number of atoms (20) in the primitive cell of $SbCrSe_3$, 60 phonon bands comprised of three acoustic branches and 57 optical branches can be obtained, in which the expected 30 Raman active modes with four inequivalent irreducible ($10A_g + 5B_{1g} + 10B_{2g} + 5B_{3g}$) are predicted. These active Raman modes are in agreement with group theory analysis, as listed in Table S4. Comparing with the DFT calculations results, the experimentally determined vibrational modes show excellent consistency. It should be noted that some modes, which are not experimentally observed, are also predicted. Moreover, the visualization of the atomic vibrations of some Raman modes (such as B_{1g}^1 ~47 cm^{-1}, A_g^2 ~58 cm^{-1} and B_{1g}^3 ~163 cm^{-1}) is displayed in Figs. 3b–d, respectively. The atomic displacement of B_{1g}^1 and B_{1g}^3 modes is along *b*-axis (out of (010)) plane, while that of A_g^2 mode belongs to in-plane (010) vibration.

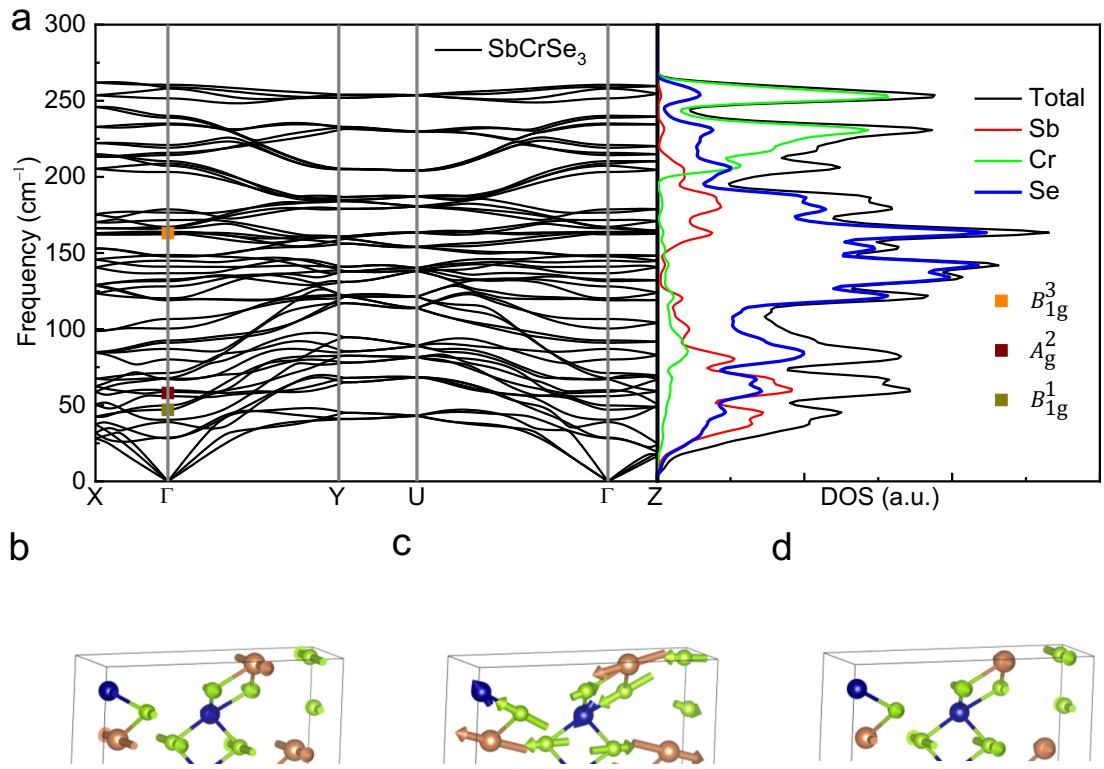

Figure 3 Phonon properties of $SbCrSe_3$. (a) The calculated phonon dispersion and density of states for $SbCrSe_3$ in left and right panels, respectively. The atomic vibrations of some Raman modes (b) B_{1g}^1 ~47 cm^{-1}, (c) A_g^2 ~58 cm^{-1} and (d) B_{1g}^3 ~163 cm^{-1}, respectively.

Anharmonic phonon decay and Thermal properties

To further elucidate the mechanisms of phonon scattering in $SbCrSe_3$ crystal, the temperature-dependent Raman spectrum was measured from 78 K to 310 K in the cleaved (00l) plane, as shown in Fig. 4a and Fig. S4. Based on the above discussion, the vibrational symmetry of each experimentally observed Raman modes can be explicitly identified, as marked in Fig. S4. All Raman peaks obviously show a red shift, and the corresponding linewidths become broadening with increasing temperature throughout the measured temperature range (Fig. 4a), which is mainly attributed to anharmonic interactions between phonons [40,41]. Here, the Raman modes B_{1g}^1 (~49 cm^{-1}) and B_{1g}^3 (~172 cm^{-1}), with the characteristics of the atomic vibration along *b*-axis, are selected to investigate inherent phonon scattering processes. Furthermore, the temperature variation of peak frequencies and FWHM of these Raman modes are

depicted in Fig. 4b and c, respectively. To commendably illustrate the temperature dependent behaviors for peak position and FWHM, the conventional model assuming the decay of an optical phonon into two (representing three phonon process) or/and three phonons (four phonon process) is applied. Therefore, the temperature dependent phonon frequency and linewidth are commonly expressed as [42]:

$$\omega = \omega_0 + A\left[1 + \frac{2}{e^{\hbar\omega_0/2k_BT}-1}\right] + B\left[1 + \frac{3}{e^{\hbar\omega_0/3k_BT}-1} + \frac{3}{(e^{\hbar\omega_0/3k_BT}-1)^2}\right] \quad (8)$$

$$\Gamma = \Gamma_0 + C\left[1 + \frac{2}{e^{\hbar\omega_0/2k_BT}-1}\right] + D\left[1 + \frac{3}{e^{\hbar\omega_0/3k_BT}-1} + \frac{3}{(e^{\hbar\omega_0/3k_BT}-1)^2}\right] \quad (9)$$

where ω_0 is the intrinsic frequency, Γ_0 the broadening at 0 K, k_B the Boltzmann constant, $\hbar$ the reduced Planck's constant and the coefficients (A, B, C and D) are the anharmonic constants.

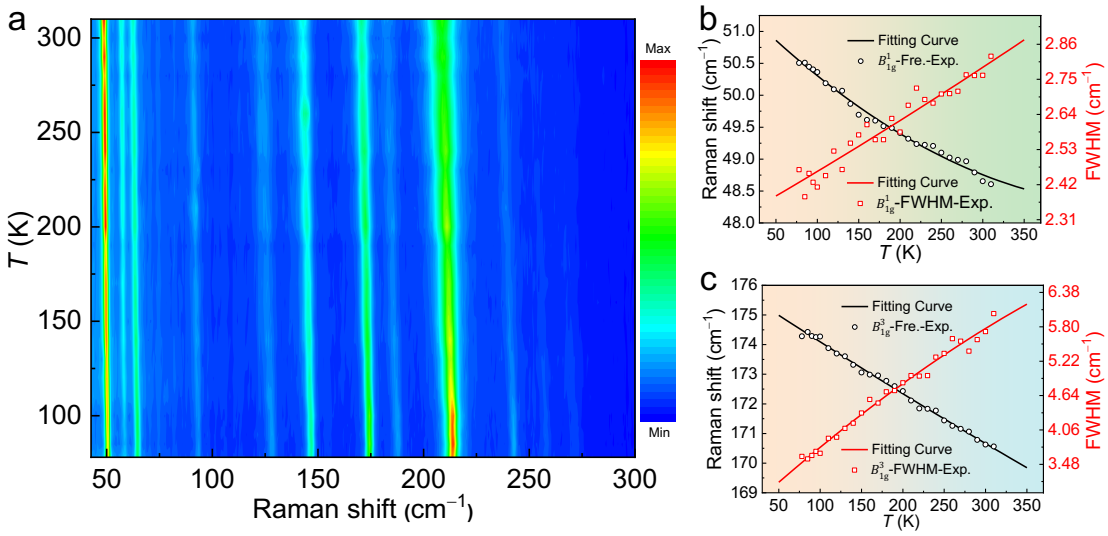

Figure 4 In-situ Raman spectra of $SbCrSe_3$. (a) Raman scattering spectrum of $SbCrSe_3$ at temperature ranging from 78 K to 310 K. The temperature dependence of the peak positions and linewidth for (b) B^1_{1g} and (c) B^3_{1g}, respectively. The red- and black-solid lines are the corresponding fitted lines.

As indicated by Fig. 4b, the fitted line on the basis of Eqs. (8) and (9) matches well with the experimental result of B^1_{1g} modes, and the relevant fitting parameters are

summarized in Table 1. Notably, compared with the obtained value of the anharmonic coefficients (*A* and *C*) with reference to three phonon process, the coefficients (*B* and *D*) involved in four phonon process can be neglected due to their small magnitude, which indicates the three-phonon interactions are dominant. Similar to the conclusion of B_{1g}^1 mode, the temperature variation of the peak position and FWHM of B_{1g}^3 mode can be well characterized by the three-phonon scattering process, as listed in Table 1. It is therefore concluded that the three-order anharmonicity in lattice potential is more accurate to describe the temperature-dependent evolution of frequency and linewidth for $SbCrSe_3$ crystal. Intriguingly, in contrast to B_{1g}^1 mode, the fitting parameters A and C shown in Table 1 for B_{1g}^3 mode exhibit relatively large values, which implies the B_{1g}^3 mode (~172 cm^{-1}) contributed by the vibrations of Se atoms has stronger anharmonic phonon-phonon coupling and thus plays a vital role in the reduction of the κ_L. In addition, the relaxation time τ for the decay process (the phonon lifetime), which is closely associated with κ_L, can be estimated by the simple relation [43], $\tau = \frac{1}{\pi c \Gamma}$, where c represents the light velocity and Γ is FWHM of Raman modes. As shown in Fig. 4b and c, the FWHM for both modes broadens with the increasing temperature, suggesting that the phonon lifetime decreases and thus leads to the decrease in κ_L with the elevated temperature. At the same time, it is evident that the change in the FWHM of B_{1g}^3 mode is significantly greater than that of B_{1g}^1 mode, which suggests the phonon lifetime of B_{1g}^3 mode drops faster with raising temperature. It is verified again that B_{1g}^3 mode plays a more important role in reducing κ_L.

Table 1 The calculated anharmonic parameters for B_{1g}^1 and B_{1g}^3 modes of $SbCrSe_3$ according to Eqs. (8) and (9), and the corresponding fitting line shown in Fig. 4b and c

Mode	ω_0 (cm^{-1})	A (cm^{-1})	B (cm^{-1})	Γ_0 (cm^{-1})	C (cm^{-1})	D (cm^{-1})
B_{1g}^1	51.48	-0.041	0.00006	2.31	0.015	0.00003

B_{1g}^3	175.92	-0.191	0.00022	2.53	0.131	-0.00061

To further explore the mechanisms of thermal transport, the thermal conductivity of $SbCrSe_3$ single crystal along *b*-axis was measured. The calculated value was also given by solving the phonon Boltzmann transport equation (BTE). Due to the $SbCrSe_3$ crystal possessing a high electrical resistivity (ρ) (Fig. S5), the electronic thermal conductivity (κ_e) is negligible, which is also found in previously reported polycrystalline samples [15]. As displayed in Fig. 5a, with increasing temperature, the experimental thermal conductivity first sharply rises to the peak value of ~15 W m^{-1} K^{-1} at 20 K and then slowly deceases to ~2 W m^{-1} K^{-1} at room temperature, suggesting the obtained $SbCrSe_3$ bulk crystal is a normal crystalline material and has intrinsically low κ_L. Unambiguously, the calculated κ_L from first principles has reasonably good agreement with the measured results of single crystal in the temperature range from 50 K to 300 K, and is slightly higher than that of the polycrystalline samples at elevated temperatures that could be owed to the absence of grain boundary and van der Waals layer interface for phonon scattering. This result substantiates that three-order anharmonicity in lattice vibration potential can well describe the thermal transport in $SbCrSe_3$, which is consistent with the conclusions obtained by the *in-situ* Raman experiment. As shown in Fig. 5b, the anharmonic scattering rates (SRs), which are inversely proportional to the phonon lifetime, are remarkably enlarged with the rising temperature, which is responsible for the temperature-dependent evolution of κ_L. In the frequency below 200 cm^{-1}, the anharmonic SRs displays a globally enhanced tendency, implying that the high frequency phonons have relatively shorter lifetime. In addition, the cumulative κ_L at 100 K and 300 K with regard to the phonon frequency is plotted in Fig. 5c. The inset of Fig. 5c shows that the contribution from optical branches for κ_L is larger than that from acoustic branches, which discloses the importance of optical branches in the thermal transport of $SbCrSe_3$ crystal. As shown in Fig. 5d, the thermal conductivities are dominated by the phonons with short mean free paths (MFPs), and the MFPs with 50% accumulation of κ_L are only ~18 nm and

5 nm at 100 K and 300 K, respectively, which indicates multiscale structural engineering should be effective to reduce κ_L [44–47].

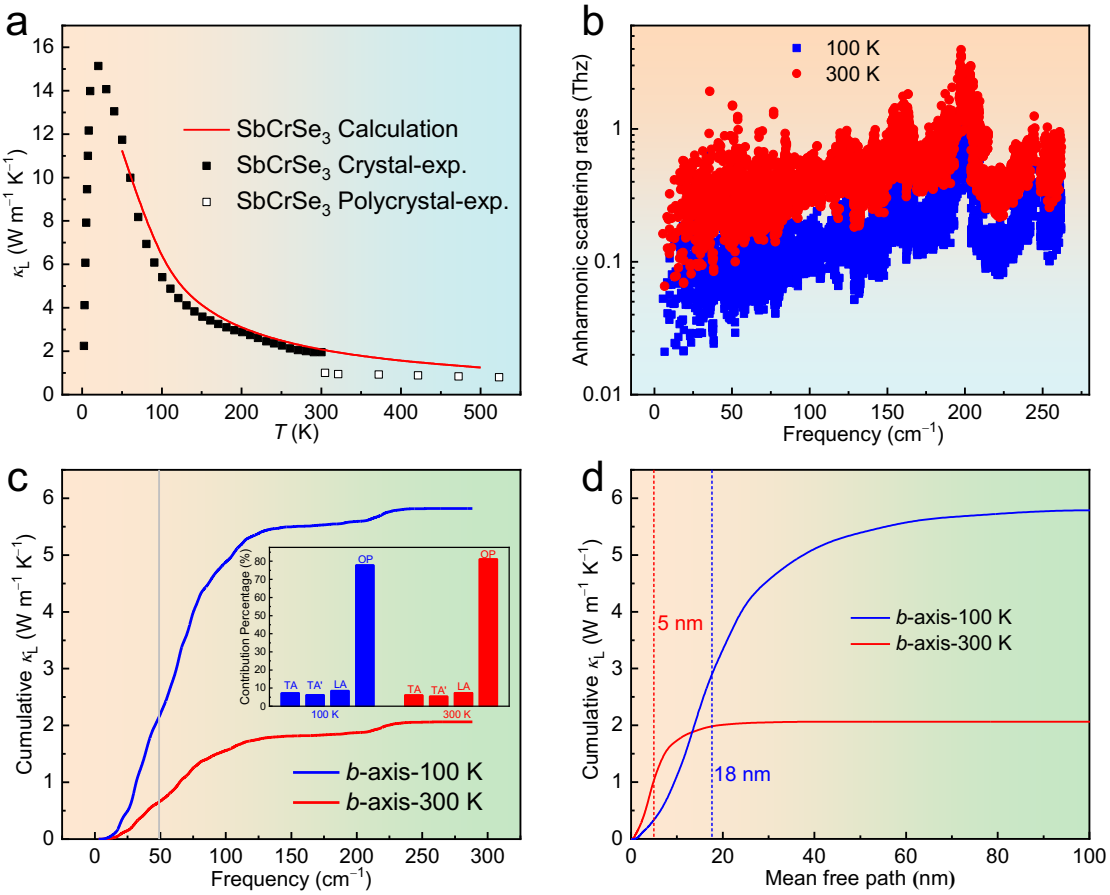

Figure 5 Thermal transport properties of $SbCrSe_3$. (a) Lattice thermal conductivity κ_L for the $SbCrSe_3$ single crystal, calculated results and polycrystalline $SbCrSe_3$ samples [15]. (b) The anharmonic SRs of $SbCrSe_3$ at 100 K and 300 K. (c) The κ_L integration for 100 K and 300 K with respect to frequency along *b*-axis, where the inset is the κ_L contribution percentage from the acoustic and optical branches. (d) The cumulative κ_L for 100 K and 300 K with regard to the phonon MFP frequency along *b*-axis.

CONCLUSIONS

In this study, bulk $SbCrSe_3$ single crystal has been successfully synthesized by self-fluxing and annealing. The long edge of fabricated needle-like crystal is undoubtedly confirmed as along *b*-axis using advanced SCXRD and HRTEM technique.

The combination of the ARPRS measurement and group theory calculation was used to identify the Raman modes symmetries for cleaved (00l) crystal plane of $SbCrSe_3$, which is further corroborated *via* DFT calculations. It is interesting to found that some modes (e.g., A_g^2 ~64 cm^{-1} and A_g^7 ~185 cm^{-1}) using the ARPRS measurement can be employed to verify the crystalline orientation of small crystals or films. In addition, facilitated by the *in-situ* Raman experiment, it is unveiled that the three phonon interactions dominate the thermal transport of $SbCrSe_3$ crystal. Furthermore, the theoretically calculated κ_L exhibits excellent agreement with the measured results, which also confirms that the approximation considering three-order term in lattice vibrational potential is reasonable. This work not only provides fundamental understanding of vibrational modes and lattice anharmonicity in the quasi-1D crystal of $SbCrSe_3$, but also describes a fast and facile method to explore the thermal transport properties of other novel low dimensional materials.

Acknowledgments

This work was financially supported in part by the National Natural Science Foundation of China (11904348, 11604032, 51772035, 51672270, 52071041), the Fundamental Research Funds for the Central Universities (106112016CDJZR308808). The work conducted at the Chongqing Institute of Green and Intelligent Technology, Chinese Academy of Sciences is also supported by Key Research Program of Frontier Sciences, CAS, (QYZDB-SSW-SLH016). We also would like to thank Ms. Guiwen Wang and Dr. Yang Zhou at Analytical and Testing Center of Chongqing University for thermal transport analysis and EPMA measurement, respectively.

Author contributions Wu H, Gong X, Lu X, Wang G and Zhou X designed the experiment and wrote the paper; Wu H, Gong X, Peng Y, Zhang L, Wang A and He M conducted experimental testing and crystal growth; Zhang B and Liu J measured the microstructure characterization; Peng K, Gu H, Han G, Chai Y and Guilmeau E participated in result analyses. All authors contributed to the general discussion.

Conflict of interest

The authors declare that they have no conflict of interest.

Supplementary information Supporting data are available in the online version of the paper.

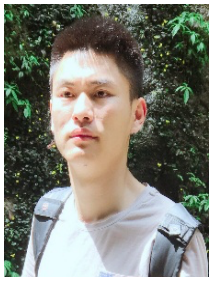

Hong Wu is a Ph.D. candidate in experimental condensed matter physics in Chongqing University. His main research is focused on the synthesis and physical properties of single crystal based thermoelectric materials and novel thermoelectric materials with low thermal conductivity.

Xiangnan Gong received his master degree in Wenzhou University (2011). Subsequently, he joined HORIBA as a senior technical engineer for Raman spectrometer. Currently, he is an engineer in Analytical and Testing Center of Chongqing University. His work and research interests mainly focus on the Raman spectroscopy of crystal structures caused by various external fields including temperature, stress and polarization.

Guoyu Wang received his Ph.D. degree in Condensed Matter Physics, University of Science and Technology of China (2007). After working as postdoc in the Hong Kong

Polytechnic University (2007–2009) and University of Michigan (2009–2012), he took a faculty position in Chongqing Institute of Green and Intelligent Technology, Chinese Academy of Sciences in 2013. His current research is focused on thermoelectric materials and strong-correlated systems. He is also interested in 3D printing technologies for metals.

Xu Lu obtained his Ph.D. in experimental condensed matter physics from the Michigan State University in 2014. After that he stayed in the same group, working as a Postdoc Fellow until August 2015. Then he joined the Department of Applied Physics, Chongqing University, China as a "100 talented Researchers of Chongqing University". His research interest focuses on thermal energy conversion materials including thermoelectric materials and low thermal conductivity materials for thermal barriers.

Xiaoyuan Zhou received her Ph.D. degree in Department of Applied Physics, Hong Kong Polytechnic University (2008). She worked as a postdoc research associate in University of Washington (2008–2010), and University of Michigan (2010–2013). In 2013, she joined Chongqing University as a professor. Her current research is focused on thermoelectric materials and their applications.

REFERENCES

[1] Chhowalla M, Jena D, Zhang H. Two-dimensional semiconductors for transistors. Nat Rev Mater, 2016, 1: 1-15

[2] Dresselhaus MS, Chen G, Tang MY, *et al.* New directions for low-dimensional thermoelectric materials. Adv Mater, 2007, 19: 1043-1053

[3] Geim AK, Grigorieva IV. Van der waals heterostructures. Nature, 2013, 499: 419-425

[4] Shivananju BN, Yu W, Liu Y, *et al.* The roadmap of graphene-based optical biochemical sensors. Adv Funct Mater, 2017, 27: 1603918

[5] Yuan H, Liu X, Afshinmanesh F, *et al.* Polarization-sensitive broadband photodetector using a black phosphorus vertical *p–n* junction. Nat Nanotechnol 2015, 10: 707-713

[6] Zhao LD, Lo SH, Zhang Y, *et al.* Ultralow thermal conductivity and high thermoelectric figure of merit in SnSe crystals. Nature, 2014, 508: 373-377

[7] Zhou X, Yan Y, Lu X, *et al.* Routes for high-performance thermoelectric materials. Mater Today, 2018, 21: 974-988

[8] Peng K, Zhang B, Wu H, *et al.* Ultra-high average figure of merit in synergistic band engineered $Sn_xNa_{1-x}Se_{0.9}S_{0.1}$ single crystals. Mater Today, 2018, 21: 501-507

[9] Gong C, Li L, Li Z, *et al.* Discovery of intrinsic ferromagnetism in two-dimensional van der waals crystals. Nature, 2017, 546: 265-269

[10] Kong T, Stolze K, Ni D, *et al.* Anisotropic magnetic properties of the ferromagnetic semiconductor $CrSbSe_3$. Phys Rev Mater, 2018, 2: 014410

[11] Mathew T, Mathew V. Density functional study of magnetic, structural and electronic properties of quasi-one-dimensional compounds $CrSbX_3$ (x = S, Se). Comput Condens Matter, 2020, 23: e00467

[12] Odink DA, Carteaux V, Payen C, *et al.* Synthesis and structure of chromium antimony triselenide ($CrSbSe_3$): A pseudo-one-dimensional ferromagnet. Chem Mater, 1993, 5: 237-240

[13] Tang X, Fan D, Peng K, *et al.* Dopant induced impurity bands and carrier concentration control for thermoelectric enhancement in *p*-type $Cr_2Ge_2Te_6$. Chem Mater, 2017, 29: 7401-7407

[14] Yang D, Yao W, Chen Q, *et al.* $Cr_2Ge_2Te_6$: High thermoelectric performance from layered structure with high symmetry. Chem Mater, 2016, 28: 1611-1615

[15] Yang D, Yao W, Yan Y, *et al.* Intrinsically low thermal conductivity from a quasi-one-dimensional crystal structure and enhanced electrical conductivity network via pb doping in $CrSbSe_3$. NPG Asia Mater, 2017, 9: e387-e387

[16] Volkov V, Van Tendeloo G, Van Landuyt J, *et al.* Hrem image analysis up to structure determination of $SbCrSe_3$: A new 1D ferromagnet. J Solid State Chem, 1997, 132: 257-266

[17] Balandin AA, Nika DL. Phononics in low-dimensional materials. Mater Today, 2012, 15: 266-275

[18] Ghosh S, Bao W, Nika DL, *et al.* Dimensional crossover of thermal transport in few-layer graphene. Nat Mater, 2010, 9: 555-558

[19] Zhang X, Tan QH, Wu JB, *et al.* Review on the Raman spectroscopy of different

types of layered materials. Nanoscale, 2016, 8: 6435-6450
[20] Wu J, Mao N, Xie L, *et al.* Identifying the crystalline orientation of black phosphorus using angle-resolved polarized Raman spectroscopy. Angew Chem Int Edit, 2015, 54: 2366-2369
[21] Li L, Wang W, Gong P, *et al.* 2D GeP: An unexploited low-symmetry semiconductor with strong in-plane anisotropy. Adv Mater, 2018, 30: 1706771
[22] Li T, Luo W, Kitadai H, *et al.* Probing the domain architecture in 2D α-Mo_2C via polarized Raman spectroscopy. Adv Mater, 2019, 31: 1807160
[23] Ribeiro HB, Pimenta MA, De Matos CJ, *et al.* Unusual angular dependence of the Raman response in black phosphorus. ACS Nano, 2015, 9: 4270-4276
[24] Zhang X, Han W, Wu J, *et al.* Raman spectroscopy of shear and layer breathing modes in multilayer MoS_2. Phys Rev B, 2013, 87: 115413
[25] Bell LE. Cooling, heating, generating power, and recovering waste heat with thermoelectric systems. Science, 2008, 321: 1457-1461
[26] Wu H, Lu X, Wang G, *et al.* Strong lattice anharmonicity securing intrinsically low lattice thermal conductivity and high performance thermoelectric $SnSb_2Te_4$ *via* Se alloying. Nano Energy, 2020, 76: 105084
[27] Shi XL, Zou J, Chen ZG. Advanced thermoelectric design: From materials and structures to devices. Chem Rev, 2020, 120: 7399-7515
[28] Wu H, Peng K, Zhang B, *et al.* Realizing high thermoelectricity in polycrystalline SnS *via* manipulating fermi surface anisotropy and phonon dispersion. Materials Today Physics, 2020, 100221
[29] Chen Z, Zhang X, Lin S, *et al.* Rationalizing phonon dispersion for lattice thermal conductivity of solids. National Science Review, 2018, 5: 888-894
[30] Xu P, Fu T, Xin J, *et al*. Anisotropic thermoelectric properties of layered compound $SnSe_2$. Science Bulletin, 2017, 62: 1663-1668
[31] Lan T, Li CW, Fultz B. Phonon anharmonicity of rutile SnO_2 studied by Raman spectrometry and first principles calculations of the kinematics of phonon-phonon interactions. Phys Rev B, 2012, 86: 134302
[32] Peercy P, Morosin B. Pressure and temperature dependences of the Raman-active phonons in SnO_2. Phys Rev B, 1973, 7: 2779
[33] Zhang S, Yang J, Xu R, *et al.* Extraordinary photoluminescence and strong temperature/angle-dependent Raman responses in few-layer phosphorene. ACS Nano, 2014, 8: 9590-9596
[34] Kresse G, Furthmüller J. Efficient iterative schemes for *ab initio* total-energy calculations using a plane-wave basis set. Phys Rev B, 1996, 54: 11169
[35] Kresse G, Joubert D. From ultrasoft pseudopotentials to the projector augmented-wave method. Phys Rev B, 1999, 59: 1758
[36] Perdew JP, Burke K, Ernzerhof M. Generalized gradient approximation made simple. Phys Rev Lett, 1996, 77: 3865
[37] Togo A, Tanaka I. First principles phonon calculations in materials science. Scripta Mater, 2015, 108: 1-5
[38] Li W, Carrete J, Katcho NA, *et al.* Shengbte: A solver of the boltzmann transport equation for phonons. Comput Phys Commun, 2014, 185: 1747-1758

[39] Loudon R. The Raman effect in crystals. Adv Phys, 1964, 13: 423-482
[40] Cuscó R, Alarcón-Lladó E, Ibanez J, *et al.* Temperature dependence of Raman scattering in ZnO. Phys Rev B, 2007, 75: 165202
[41] Domènech-Amador N, Cuscó R, Artus L, *et al.* Raman scattering study of anharmonic phonon decay in InN. Phys Rev B, 2011, 83: 245203
[42] Balkanski M, Wallis R, Haro E. Anharmonic effects in light scattering due to optical phonons in silicon. Phys Rev B, 1983, 28: 1928
[43] Chen LC, Cao ZY, Yu H, *et al.* Phonon anharmonicity in thermoelectric palladium sulfide by Raman spectroscopy. Appl Phys Lett, 2018, 113: 022105
[44] Huang L, Lu J, Ma D, *et al.* Facile *in situ* solution synthesis of SnSe/rGO nanocomposites with enhanced thermoelectric performance. J Mater Chem A, 2020, 8: 1394-1402
[45] Li JF, Liu WS, Zhao LD, *et al.* High-performance nanostructured thermoelectric materials. NPG Asia Mater, 2010, 2: 152-158
[46] Shen XC, Zhang X, Zhang B, *et al.* Optimizing thermoelectric properties of BiSe through Cu additive enhanced effective mass and phonon scattering. Rare Metals, 2020, 39: 1374-1382.
[47] Zhang A, Zhang B, Lu W, *et al*. Twin engineering in solution-synthesized nonstoichiometric Cu5FeS_4 icosahedral nanoparticles for enhanced thermoelectric performance. Adv Funct Mater, 2018, 28: 1705117

拉曼光谱定义$SbCrSe_3$单晶的振动模式对称性和声子非谐性

吴宏[1,2,†]，公祥南[3,†]，彭义[4]，张龙[1]，张斌[3]，彭坤玲[1]，刘杰[3]，韩广[5]，王爱峰[1]，柴一晟[1]，何明全[1]，顾豪爽[4]，Emmanuel Guilmeau[6]，王国玉[2,*]，卢旭[1,*]，周小元[1,3,*]

摘要：本文报道了 $SbCrSe_3$ 单晶的合成方法及其在 2–300 K 温度范围内的热输运性能。通过角分辨偏振拉曼光谱技术、群论和理论计算分析，我们首次定义了该晶体沿(00l)解理面的拉曼振动模式对称性，并可利用其某些模式确定晶体轴向。另外，通过原位变温拉曼光谱和理论计算相结合的方式，分析得出三声子散射过程即可准确地描述晶格热导率对温度的依赖关系。本文从一个全新的角度揭示了 $SbCrSe_3$ 的热输运性质，为研究其他低维材料热性能提供有力借鉴。

Graphical Abstract

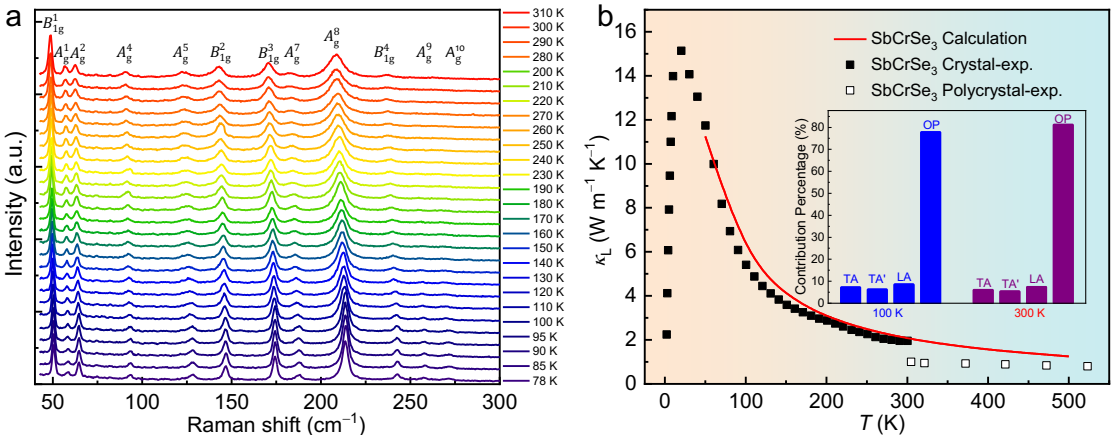

SCIENCE CHINA Materials

Supporting Information

Identification of vibrational mode symmetry and phonon anharmonicity in $SbCrSe_3$ single crystal using Raman spectroscopy

Hong Wu[1,2,†], Xiangnan Gong[3,†], Yi Peng[4], Long Zhang[1], Bin Zhang[3], Kunling Peng[1], Jie Liu[3], Guang Han[5], Aifeng Wang[1], Yisheng Chai[1], Mingquan He[1], Haoshuang Gu[4], Emmanuel Guilmeau[6], Guoyu Wang[2,*], Xu Lu[1,*] and Xiaoyuan Zhou[1,3,*]

[1] College of Physics and Institute of Advanced Interdisciplinary Studies, Chongqing University, Chongqing 401331, China

[2] Chongqing Institute of Green and Intelligent Technology, Chinese Academy of Sciences, Chongqing 400714, China

[3] Analytical and Testing Center of Chongqing University, Chongqing 401331, China

[4] Hubei Collaborative Innovation Center for Advanced Organic Chemical Materials, Hubei Key Laboratory of Ferro & Piezoelectric Materials and Devices, Faculty of Physics & Electronic Sciences, Hubei University, Wuhan 430062, China

[5] College of Materials Science and Engineering, Chongqing University, Chongqing 400044, China

[6] Laboratoire CRISMAT, UMR-CNRS, Normandie University, Caen 14050, France

[†] These authors contributed equally to this work.

[*] Corresponding authors (emails: guoyuw@cigit.ac.cn (Wang G); luxu@cqu.edu.cn (Lu X); xiaoyuan2013@cqu.edu.cn (Zhou X))

Section I. Raman theory

The intensity (I) of the observed Raman vibration modes can be expressed as:

$$\mathrm{I} \propto \left|\vec{e}_i \cdot \vec{M} \cdot \vec{R} \cdot \vec{M}^{-1} \cdot \vec{e}_s\right|^2$$

The Raman tensors of A_g, $B_{1\mathrm{g}}$, $B_{2\mathrm{g}}$ and $B_{3\mathrm{g}}$ according to the $D_{2\mathrm{h}}$ point group can be expressed as:

$$\vec{R}(A_\mathrm{g}) = \begin{pmatrix} ae^{i\varphi_a} & 0 & 0 \\ 0 & be^{i\varphi_b} & 0 \\ 0 & 0 & ce^{i\varphi_c} \end{pmatrix}, \quad \vec{R}(B_{1\mathrm{g}}) = \begin{pmatrix} 0 & de^{i\varphi_d} & 0 \\ de^{i\varphi_d} & 0 & 0 \\ 0 & 0 & 0 \end{pmatrix}$$

$$\vec{R}(B_{2\mathrm{g}}) = \begin{pmatrix} 0 & 0 & ee^{i\varphi_e} \\ 0 & 0 & 0 \\ ee^{i\varphi_e} & 0 & 0 \end{pmatrix}, \qquad \vec{R}(B_{3\mathrm{g}}) = \begin{pmatrix} 0 & 0 & 0 \\ 0 & 0 & fe^{i\varphi_f} \\ 0 & fe^{i\varphi_f} & 0 \end{pmatrix}$$

When the incident laser propagates along the $\overline{x}$ direction with unit polarization vector along y-axis ($\vec{e}_i = (0\ 1\ 0)$). The orthogonal transform matrix is obtained by:

$$\vec{M} = \begin{pmatrix} 1 & 0 & 0 \\ 0 & cos\theta & sin\theta \\ 0 & -sin\theta & cos\theta \end{pmatrix}$$

For the selectivity analyzer with unit polarization vector $\vec{e}_s{}^{\mathrm{T}} = (0\ 1\ 0)$ defined as parallel configuration, the Raman scattering intensities of different modes can be expressed as:

$$I(A_\mathrm{g}, \|) \propto |c|^2 \cdot sin^4\theta + |b|^2 \cdot cos^4\theta + 2|c||b| \cdot cos\varphi_{bc} \cdot sin^2\theta \cdot cos^2\theta \quad \mathrm{S(1)}$$

$$I(B_{3\mathrm{g}}, \|) \propto f^2 \cdot sin^2 2\theta \quad \mathrm{S(2)}$$

In perpendicular configuration, the selectivity analyzer has unit polarization vector $\vec{e}_s{}^{T} = (0\ 0\ 1)$. The Raman scattering intensities of different modes can be expressed as:

$$\mathrm{I}(A_\mathrm{g}, \perp) \propto \tfrac{1}{4} \cdot sin^2 2\theta \cdot (|c|^2 - 2|c||b| \cdot cos\varphi_{bc} + |b|^2) \quad \mathrm{S(3)}$$

$$I(B_{3\mathrm{g}}, \perp) \propto f^2 \cdot cos^2 2\theta \quad \mathrm{S(4)}$$

where $\varphi_{bc} = \varphi_b - \varphi_c$ is the phase difference.

When the incident laser propagates along the $\overline{y}$ direction with unit polarization vector

along z-axis ($\vec{e}_i = (0\ 0\ 1)$). The orthogonal transform matrix is obtained by:

$$\vec{M} = \begin{pmatrix} cos\theta & 0 & -sin\theta \\ 0 & 1 & 0 \\ sin\theta & 0 & cos\theta \end{pmatrix}$$

For the selectivity analyzer with unit polarization vector $\vec{e}_s{}^{\mathrm{T}} = (0\ 0\ 1)$ defined as parallel configuration, the Raman scattering intensities of different modes can be expressed as:

$$\mathrm{I}\left(A_{\mathrm{g}}, \|\right) \propto |a|^2 \cdot sin^4\theta + |c|^2 \cdot cos^4\theta + 2|c||a| \cdot cos\varphi_{ac} \cdot sin^2\theta \cdot cos^2\theta \quad \mathrm{S}(5)$$

$$\mathrm{I}\left(B_{2\mathrm{g}}, \|\right) \propto e^2 \cdot sin^2 2\theta \quad \mathrm{S}(6)$$

On perpendicular configuration, the selectivity analyzer has unit polarization vector $\vec{e}_s{}^{\mathrm{T}} = (1\ 0\ 0)$. The Raman scattering intensities of different modes can be expressed as:

$$\mathrm{I}(A_{\mathrm{g}}, \perp) \propto \frac{1}{4} \cdot sin^2 2\theta \cdot (|a|^2 - 2|c||a| \cdot cos\varphi_{ac} + |c|^2) \quad \mathrm{S}(7)$$

$$\mathrm{I}(B_{2\mathrm{g}}, \perp) \propto e^2 \cdot cos^2 2\theta \quad \mathrm{S}(8)$$

where $\varphi_{ac} = \varphi_a - \varphi_c$ is the phase difference.

Section II. Figures

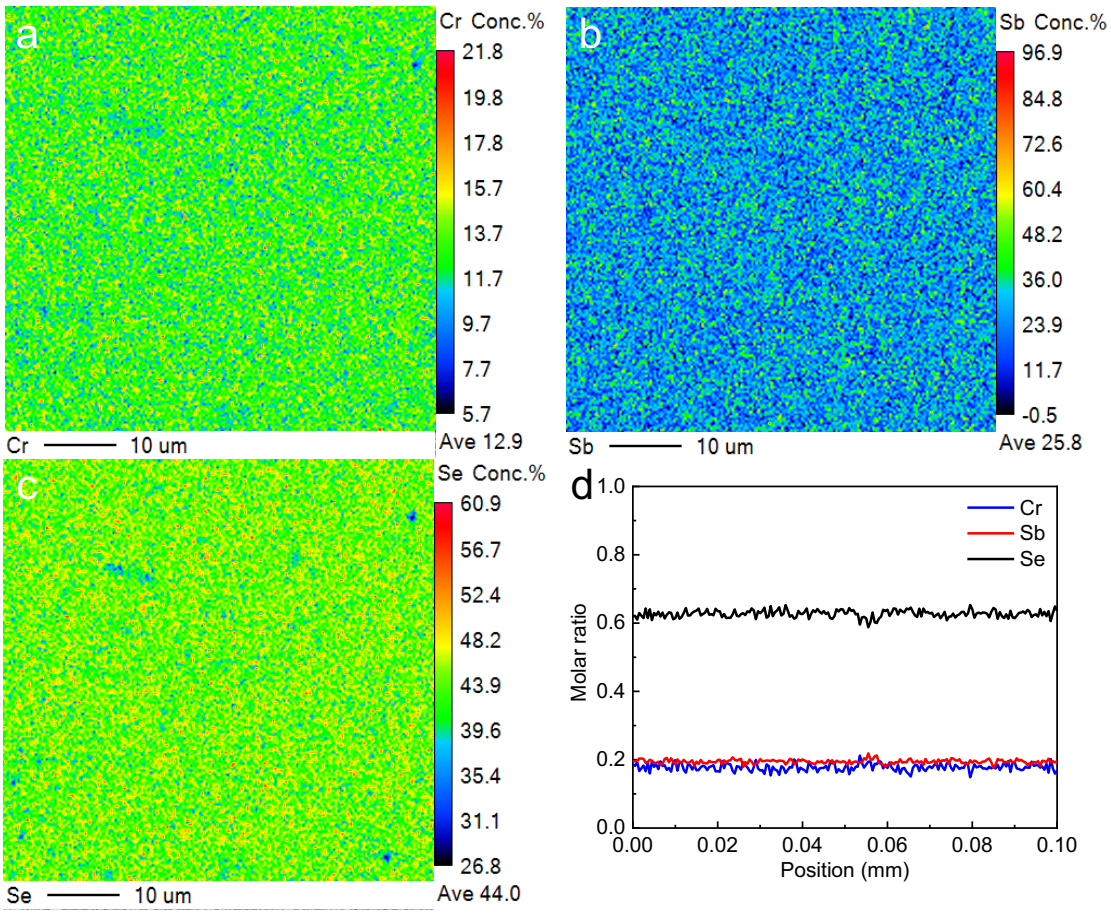

Figure S1 (a)–(c) The EPMA images corroborates the chemical homogeneity of $SbCrSe_3$ crystal. (d) The corresponding stoichiometric ratio is consistent with nominal component.

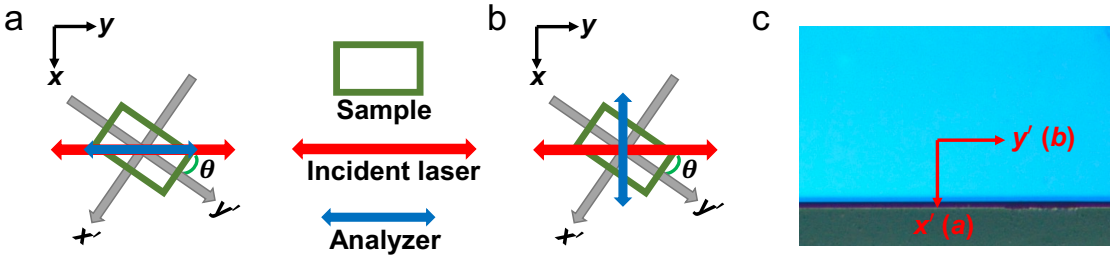

Figure S2 (a) Schematic diagram for parallel configuration. (b) Schematic diagram for perpendicular configuration. (c) The sample under an optical microscope shows x' (a) -axis and y' (b) -axis.

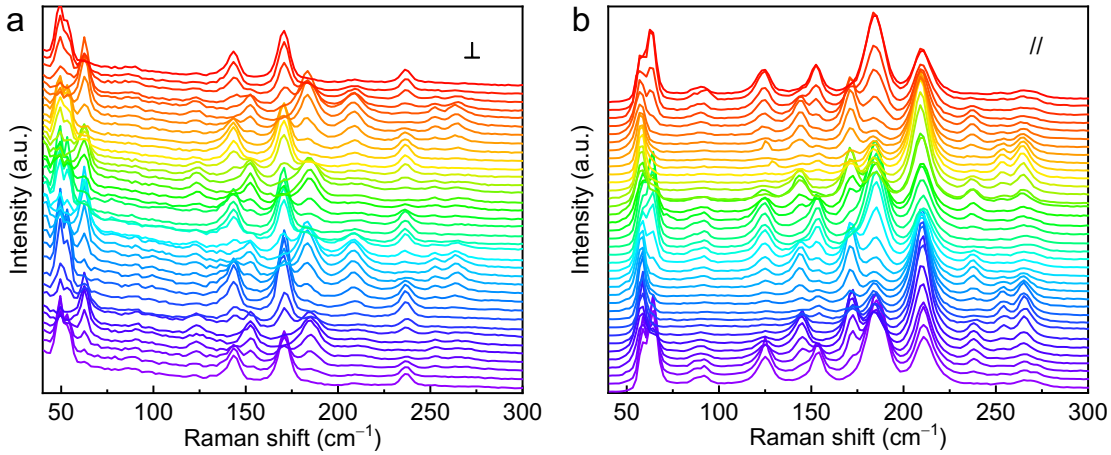

Figure S3 Typical polarized Raman spectra for (a) and (b) in perpendicular and parallel configuration, respectively, where the different curves correspond to the various angles. From bottom to top, the angles change from 0° to 360° with 10° intervals.

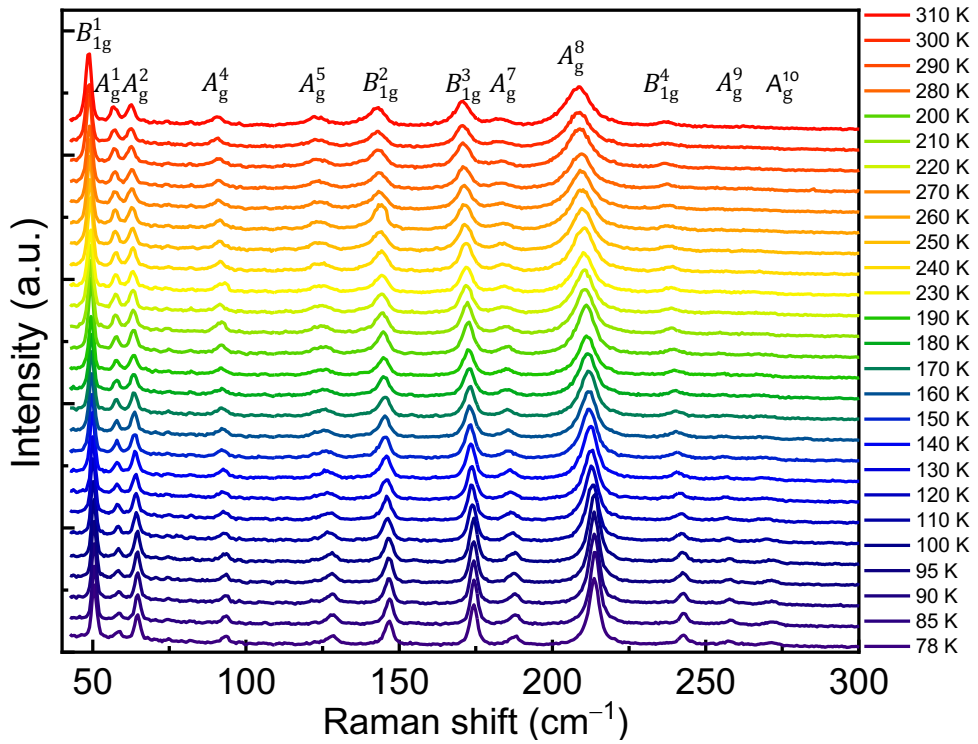

Figure S4 The temperature dependence of Raman spectra of $SbCrSe_3$ in the varied temperature range from 78 to 310 K.

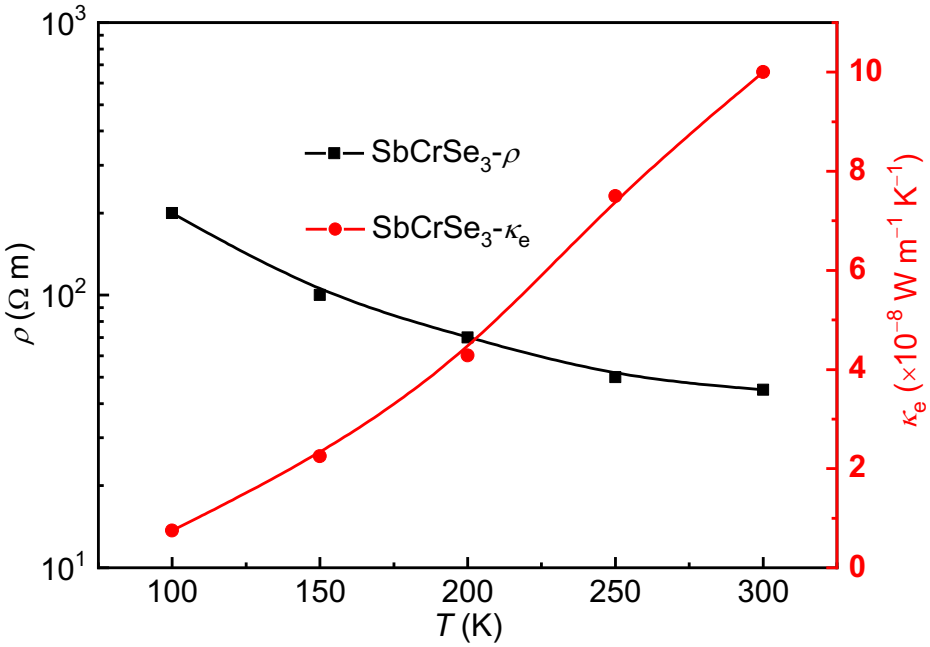

Figure S5 The temperature-dependent ρ and κ_e of $SbCrSe_3$ crystal.

Section III. Tables

Table S1 Crystal data and structure refinement for $SbCrSe_3$

Empirical formula	$SbCrSe_3$
Formula weight	410.63
Temperature/K	295(2)
Crystal system	orthorhombic
Space group	*Pnma*
a/Å	9.1475(6)
b/Å	3.7872(3)
c/Å	13.4264(11)
α/°	90
β/°	90
γ/°	90
Vomule/Å^3	465.14(6)
Z	4
ρ_{calc}g/cm^3	5.864
μ/mm^{-1}	31.414
F(000)	708.0
Crystal size/mm^3	0.38 × 0.12 × 0.11
Radiation/Å	Mo Kα (λ = 0.71073)
2θ range for data collection/°	7.53 to 57.634
Index ranges	−4 ≤ h ≤ 12, −4 ≤ k ≤ 4, −5 ≤ l ≤16
Reflections collected	1222
Independent reflections	617 [R_{int} = 0.0224, R_{sigma} = 0.0375]
Data/restraints/parameters	617 / 0 / 31
Goodness-of-fit on F^2	1.122
Final R indexes [I>=2σ(I)]	R_1 = 0.0392, wR_2 = 0.1000
Final R indexes [all data]	R_1 = 0.0443, wR_2 = 0.1057
Largest diff. peak/hole/e Å^{-3}	2.40 / −1.80

Table S2 The angle dependence of Raman peak intensities for each Raman active modes of $SbCrSe_3$ with exposed (100), (010) and (001) plane in cross- and parallel-polarized configuration

Mode	$I_{//}^{100}$	$I_{\perp}^{100}$	$I_{//}^{010}$	$I_{\perp}^{010}$	$I_{//}^{001}$	$I_{\perp}^{001}$
A_g	Eq. S(1)	Eq. S(3)	Eq. S(5)	Eq. S(7)	Eq. (5)	Eq. (4)
B_{1g}	0	0	0	0	Eq. (7)	Eq. (6)
B_{2g}	0	0	Eq. S(6)	Eq. S(8)	0	0
B_{3g}	Eq. S(2)	Eq. S(4)	0	0	0	0

Table S3 The ARPRS intensities in parallel and perpendicular polarization configurations (the red and blue lines represent B_{1g} and A_g modes, respectively)

Peak [cm^{-1}]	49 (B_{1g}^1)		58 (A_g^1)		64 (A_g^2)	
	//	⊥	//	⊥	//	⊥
	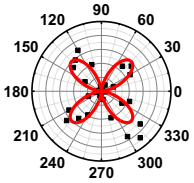	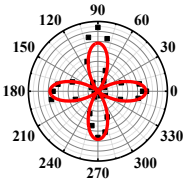	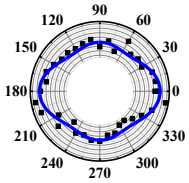	Undistinguishable	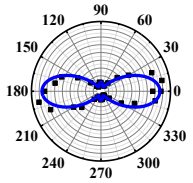	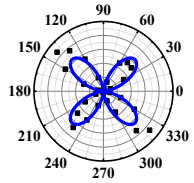
Peak [cm^{-1}]	89 (A_g^3)		92 (A_g^4)		125 (A_g^5)	
	//	⊥	//	⊥	//	⊥
	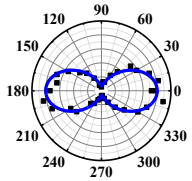	Weak	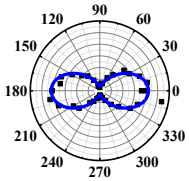	Weak	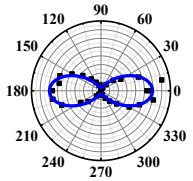	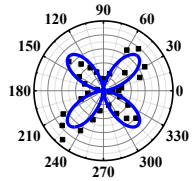
Peak [cm^{-1}]	144 (B_{1g}^2)		153 (A_g^6)		172 (B_{1g}^3)	
	//	⊥	//	⊥	//	⊥

	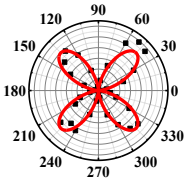	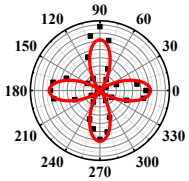	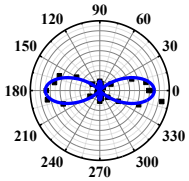	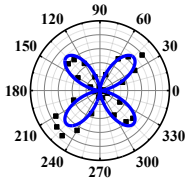	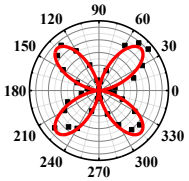	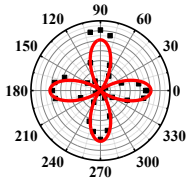
Peak [cm^{-1}]	185 (A_g^7)		209 (A_g^8)		238 (B_{1g}^4)	
	//	⊥	//	⊥	//	⊥
	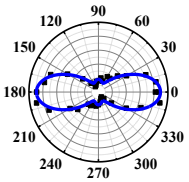	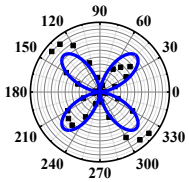	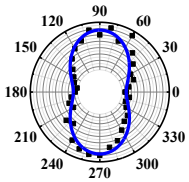	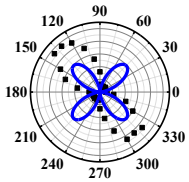	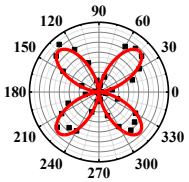	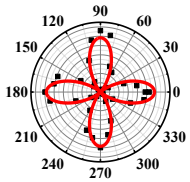
Peak [cm^{-1}]	254 (A_g^9)		265 (A_g^{10})			
	//	⊥	//	⊥		
	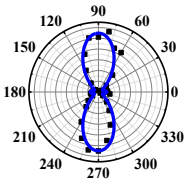	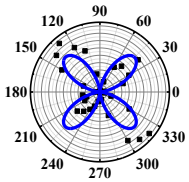	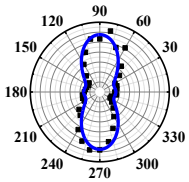	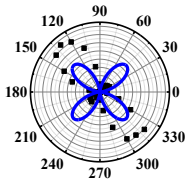		

Table S4 Experimental Raman peak frequencies (in cm^{-1}) and vibrational symmetries of $SbCrSe_3$. The predicted values of peak frequency given by DFT calculations are also listed for comparison. The B_{2g}^{x} and B_{3g}^{x} are also well predicted

Exp.	**Symmetry**	**DFT**	**Symmetry**	**DFT**
49	B_{1g}^{1}	47	B_{3g}^{1}	49
58	A_{g}^{1}	55	B_{2g}^{1}	59
64	A_{g}^{2}	58	B_{2g}^{2}	67
89	A_{g}^{3}	87	B_{2g}^{3}	80
92	A_{g}^{4}	/	B_{3g}^{2}	92
125	A_{g}^{5}	120	B_{2g}^{4}	128
144	B_{1g}^{2}	131	B_{3g}^{3}	132
153	A_{g}^{6}	149	B_{2g}^{5}	148
172	B_{1g}^{3}	163	B_{3g}^{4}	163
185	A_{g}^{7}	171/176	B_{2g}^{6}	166
209	A_{g}^{8}	203	B_{2g}^{7}	178
238	B_{1g}^{4}	215	B_{2g}^{8}	208
254	A_{g}^{9}	235	B_{3g}^{5}	214
265	A_{g}^{10}	251	B_{2g}^{9}	234
			B_{2g}^{10}	257